Electrochimica Acta 364 (2020) 137164

Contents lists available at ScienceDirect

Electrochimica Acta

journal homepage: www.elsevier.com/locate/electacta

Controllable low-temperature growth and enhanced photoelectrochemical water splitting of vertical SnS_2 nanosheets on graphene

Dong-Bum Seo, Min-Song Kim, Tran Nam Trung, Eui-Tae Kim*

Department of Materials Science & Engineering, Chungnam National University, Daejeon 34134, Republic of Korea

ARTICLE INFO

Article history:
Received 20 June 2020
Revised 25 August 2020
Accepted 21 September 2020
Available online 25 September 2020

Keywords:
Photoelectrochemistry
SnS_2
Graphene
Nanosheets
Chemical vapor deposition

ABSTRACT

Two-dimensional (2D) SnS_2 nanosheets vertically grown on graphene electrodes have still not been demonstrated despite their considerable research interest and potential for photoelectrochemical (PEC) applications. Herein, the controllable growth and enhanced PEC water-splitting performance of vertically aligned 2D SnS_2 nanosheets on graphene are reported. The heterojunction quality of the graphene/2D SnS_2 nanosheets was ensured by low-temperature growth at 230 °C using metalorganic chemical vapor deposition, resulting in significantly improved charge transfer properties. The PEC photocurrent density and photoconversion efficiency significantly increased upon insertion of a graphene layer. In addition, the 2D SnS_2 nanosheet microscopic structure dependency of the PEC performance was systematically studied. The best PEC reactivity of the 2D SnS_2 nanosheets was achieved at a height of ~0.85 µm, corresponding to nearly the limit of the carrier diffusion length, and a thickness of ~70 nm to balance the low interfacial contact resistance with an effective photogenerated carrier dynamics. These results, including the low-temperature vertical growth of 2D SnS_2 on graphene, can effectively be utilized to exploit the full potential of 2D SnS_2 for various PEC applications.

1. Introduction

Photoelectrochemical (PEC) water splitting has attracted considerable attention as a promising eco-friendly technology for converting solar energy to clean hydrogen fuel [1–3]. Numerous semiconductors, including oxides and metal chalcogenides, have been extensively studied for PEC photoelectrode applications [3]. Recently, graphene-like two-dimensional (2D) metal dichalcogenides, such as SnS_2, MoS_2, and WSe_2, have emerged as promising semiconductor photocatalysts owing to their strong photoexcitation, good chemical stability, and earth abundance [4–7]. 2D SnS_2 is of particular interest due to its appropriate bandgap energy of 2.18–2.44 eV, high carrier mobility (~300 $cm^2\ V^{-1}\ s^{-1}$ for 3-nm-thick SnS_2), high optical absorption, and strong photocatalytic activity [7,8]. SnS_2, an n-type semiconductor, is generally utilized as a photoanode, at which an oxygen evolution reaction (OER: $H_2O \rightarrow 2H^+ + ½O_2 + 2e^-$) occurs, whereas a hydrogen evolution reaction (HER: $2H^+ + 2e^- \rightarrow H_2$) occurs at the counter cathode, e.g., Pt. The appropriate design of 2D SnS_2 nanosheets on conductive substrates in terms of physical nanostructure architecture and the energy band diagram is the decisive factor for improving photogeneration and transportation of charge carriers to electrode/liquid interfaces, consequently enhancing the OER and HER.

The ideal architecture of 2D SnS_2 nanosheets on conductive substrates involves vertically standing 2D SnS_2 structures. The vertically standing 2D SnS_2 structure has recently been reported to significantly enhance the PEC performance because of its higher specific surface area of catalytic sites and stronger light absorption by multiple photon scattering effect than a horizontal structure [9]. Additionally, the highly conductive edges of 2D SnS_2 nanosheets provide an efficient pathway for photoexcited carriers and good electronic contact with substrates. Recently, various synthesis methods, including chemical vapor deposition (CVD), hydrothermal reaction, and close space sublimation, have been utilized to synthesize SnS_2 nanosheets that vertically stand on substrates [9–15]. However, the methods have generally used solid powders as Sn and S precursors, such as stannic chloride ($SnCl_4{\cdot}5H_2O$), SnS_2, and S powders, which have high melting and boiling temperatures. As a result, 2D SnS_2 nanosheets have been formed at high growth temperatures near 450 °C, which considerably limit the conducting substrate choice. Essentially, further lowering the growth temperature will provide a useful path to exploit the benefits of various promising heterojunctions, such as vertically aligned 2D SnS_2 on graphene. Graphene has emerged

---

* Corresponding author.
E-mail address: etkim@cnu.ac.kr (E.-T. Kim).

https://doi.org/10.1016/j.electacta.2020.137164

as one of the most fascinating conductive layers, exhibiting a remarkable electron mobility (>15,000 $cm^2\ V^{-1}\ s^{-1}$) [16]. Liu et al. recently demonstrated the synthesis of vertically aligned SnS_2 nanosheets on carbon cloth substrates for PEC water splitting [9]. SnS_2/graphene nanocomposites have also been studied as a high rate anode material for lithium battery [17,18]. In addition, graphene and its derivatives have been extensively studied for various promising applications, including in-vivo bioimaging of AgInZnS–graphene oxide (GO) nanocomposites [19], X-ray photon detection of $CsPbBr_3$/reduced GO nanocomposites [20], and light-controlled conductive switching of Cu_2O/reduced GO nanocomposites [21]. Despite the considerable interest in and potential of 2D heterojunction systems, the growth and PEC performance of vertically aligned 2D SnS_2 on graphene have not been demonstrated thus far. The graphene/SnS_2 junction quality can crucially deteriorate owing to the high growth temperature of 2D SnS_2 because graphene is just one or two layers of sp^2-bonded carbons. Thus, it is essential to grow 2D SnS_2 at a low temperature in order to minimize the structural and chemical destruction of the graphene layer.

Additionally, the microscopic structure of 2D SnS_2 nanosheets, such as the height and thickness, significantly affects the electrochemical OER and HER performance. Velicky et al. reported a strong dependence of charge transfer kinetics and PEC activity on the layer thickness of 2D MoS_2 [22]. Bulk MoS_2 exhibited faster charge transfer kinetics than monolayer MoS_2 because of its stronger total light absorption, which strongly depends on the number of MoS_2 layers. Moreover, bulk MoS_2 also yielded a higher PEC photocurrent than few-layer and monolayer MoS_2. Although the comparison was based on horizontal 2D MoS_2 structures on substrates, the results suggested that the structural optimization of 2D SnS_2 nanosheets is central for exploiting the full potential of vertically aligned 2D SnS_2 nanosheets for efficient PEC applications. However, little information is available on the structural optimization of vertically aligned 2D SnS_2 for efficient carrier transfer and the corresponding PEC properties.

Herein, we report the significantly enhanced PEC performance of 2D SnS_2 nanosheets that were vertically grown on graphene substrates via metalorganic CVD (MOCVD) at a low temperature of 230 °C. We successfully manipulated the microscopic structure of 2D SnS_2 nanosheets, including the thickness and height, in a controllable and practical manner by varying the ratio of Sn and S precursors. We determined the optimal structure of 2D SnS_2 nanosheets for efficient charge transfer and PEC performance via a systematic study on various microscopic structures. The PEC performance of the optimized 2D SnS_2 nanosheets was further improved upon insertion of a graphene layer.

2. Experimental

Graphene was synthesized on Cu foils (Alfa Aesar) using inductively coupled plasma (ICP) CVD with CH_4 and H_2 gases at 950 °C for 5 min. The ICP power and growth pressure were fixed at 200 W and 1 Torr, respectively. The synthesized graphene on Cu was transferred to an indium tin oxide (ITO) glass substrate. The CVD growth and transfer procedures of graphene were described in further detail elsewhere [23]. 2D SnS_2 was grown on ITO and ITO/graphene substrates at 230 °C at a pressure of 8 Torr for 15 min using a MOCVD system with $SnCl_4$ and H_2S gas (5 vol.% in a balance of N_2) as Sn and S precursors, respectively (Fig. 1). $SnCl_4$ was vaporized at 7 °C and was then delivered into a quartz reaction tube using Ar gas. The flow rate ratios of the Ar carrier to H_2S gases were varied as 150:50, 125:75, 100:100, and 75:125, where the total flow rate of the gases was fixed at 200 SCCM (standard cubic centimeters per minute).

The 2D SnS_2 morphology was characterized via scanning electron microscopy (SEM, Hitachi S-4800). The micro- and crystal structures of SnS_2 were investigated using transmission electron microscopy (TEM, Tecnai G^2 F30 S-Twin), X-ray diffraction (XRD, Bruker AXS D8 Discover), and micro-Raman spectroscopy using an excitation band of 532 nm and a charge-coupled device detector. The optical properties were evaluated using an ultraviolet–visible (UV–vis) spectrophotometer (S-3100, SCINCO). The chemical states and sample compositions were characterized by X-ray photoelectron spectroscopy (XPS, Thermo Fisher K-Alpha+). The photoexcited carrier behavior was investigated by time-resolved photoluminescence (TRPL) measurements. The energy level of SnS_2 was evaluated via UV photoelectron spectroscopy (UPS; Thermo scientific, K-alpha$^+$).

PEC cells were fabricated on $1 \times 2\ cm^2$ ITO and ITO/graphene substrates. The working area of the PEC photo-electrode was fixed at $0.5 \times 0.5\ cm^2$ using nonconductive epoxy to cover the undesired area [24,25]. PEC characterization was performed using a three-electrode system and an electrochemical analyzer (potentiostat/galvanostat 263A). A Pt plate and KCl-saturated calomel (Hg/Hg_2Cl_2) were used as the counter and reference electrodes, respectively. The electrolyte solution was 0.5 M Na_2SO_4. The light source used was a 150-W Xe arc lamp that delivered an intensity of 100 mW/cm^2 of simulated AM 1.5 G irradiation. The current–voltage characteristics were recorded using a sourcemeter (Keithley 2400). Electrochemical impedance spectroscopy (EIS) measurements were performed under dark and constant light illumination (100 mW/cm^2) at a bias of 1.0 V while varying the AC frequency in the range from 100 kHz to 100 mHz. The incident monochromatic photon-to-current conversion efficiency (IPCE) of the electrode structure was measured using a grating monochromator in the excitation wavelength range of 300–700 nm.

3. Results and discussion

The microscopic structure of 2D SnS_2 was manipulated by the flow rate ratio of the Ar carrier gas to H_2S gas in a well-controlled manner (Figs. 2 and S1 in Supporting Information). The highest ratio of $SnCl_4/H_2S$ (150:50 as the Ar carrier gas/H_2S flow rate ratio) produced the thinnest SnS_2 nanosheets with an average thickness of ~25 nm on an ITO substrate, which is hereinafter referred to as 2D SnS_2-S (Fig. 2a). The average height and width of the SnS_2 nanosheets were ~0.5 µm and ~1.0 µm, respectively. Upon decreasing the ratio of $SnCl_4/H_2S$, the SnS_2 nanosheets became larger and thicker. For a gas ratio of 125:75, the 2D SnS_2 nanosheets appeared to be ~70 nm, ~0.85 µm, and ~2.0 µm in terms of thickness, height, and width, respectively, which is hereinafter referred to as 2D SnS_2−M (Fig. 2b). Upon further decreasing the gas ratio to 100:100, the 2D SnS_2 nanosheets became larger, ~130 nm in thickness, ~1.3 µm in height, and ~2.5 µm in width, which is hereinafter referred to as 2D SnS_2-L (Fig. 2c). For the gas ratio of 75:125, the thickness and height of 2D SnS_2 nanosheets increased further to ~220 nm and ~1.5 µm, respectively, while the width remained almost unchanged at ~2.5 µm, which is hereinafter referred to as 2D SnS_2-VL (Fig. 2d). The growth behavior implies that the H_2S gas may be a crucial facilitator for enhancing the chemical reaction, i.e., $SnCl_4\ (v) + 2\ H_2S\ (g) \rightarrow SnS_2\ (s) + 4\ HCl\ (g)$, at such a low growth temperature [26]. The width of the 2D SnS_2 nanosheets seemed to be self-constrained by being blockaded by other growing 2D nanosheets, as seen in 2D SnS_2-L sample. The height and thickness of 2D SnS_2 nanosheets were then further increased at the gas ratio of 75:125 (2D SnS_2-VL).

The 2D SnS_2 nanosheets showed typical XRD patterns of hexagonal SnS_2 regardless of the gas ratios of $SnCl_4/H_2S$ (Fig. 3a). The diffraction peaks at $2\theta = 15.0°$, 28.2°, 30.4°, 32.1°, 41.8°, 45.6°, 49.9°, and 52.4° can be attributed to the (001), (100), (002), (011),

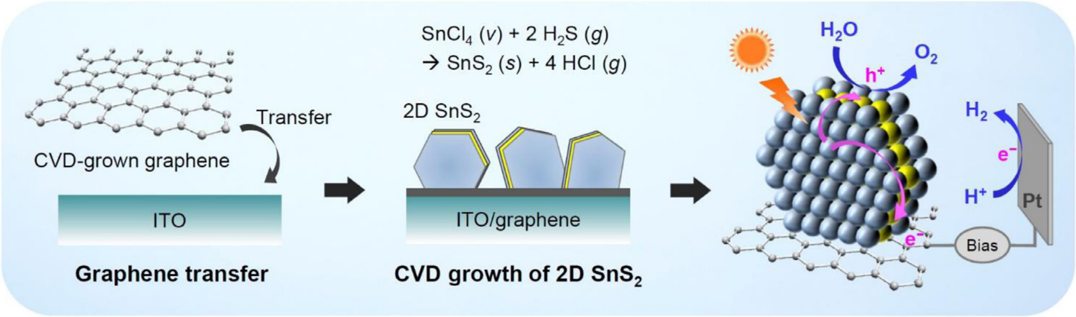

Fig. 1. Schematic of the preparation method for vertically aligned 2D SnS_2 nanosheets on graphene.

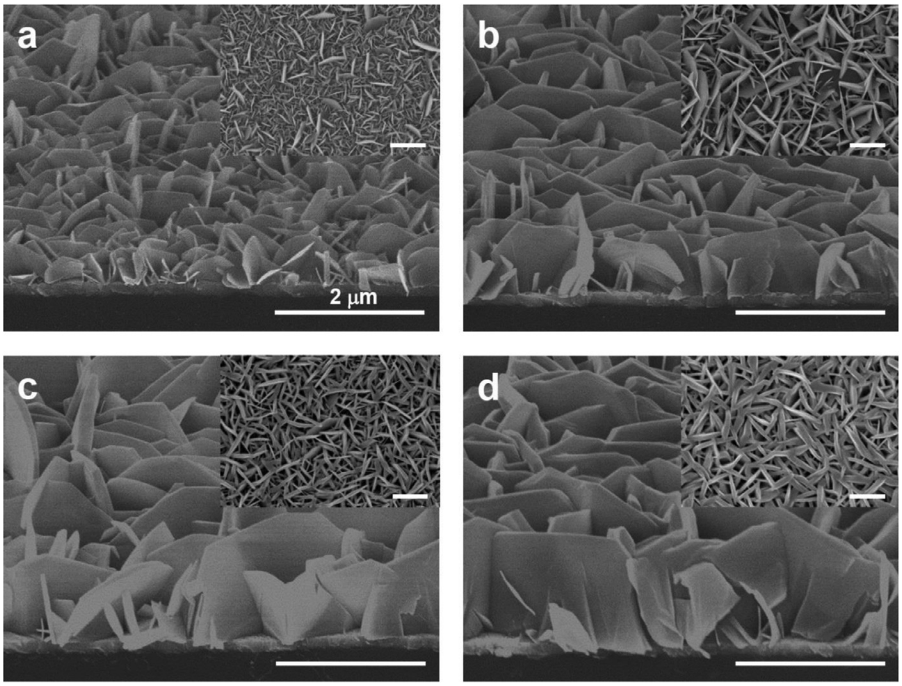

Fig. 2. SEM image of 2D SnS_2 nanosheets vertically grown on ITO substrates: (a) 2D SnS_2-S, (b) 2D SnS_2−M, (c) 2D SnS_2-L, and (d) 2D SnS_2-VL. The insets show the corresponding planar-view SEM images. Scale bar is 2 µm.

(012), (003), (110), and (111) planes of the hexagonal structure of 2H-SnS_2 (JCPDS No. 89-2358). 2D SnS_2-S and 2D SnS_2−M exhibited the preferential (001) peak. With the increasing size of SnS_2 nanosheets (2D SnS_2-L and 2D SnS_2-VL), the (100) peak, corresponding to the vertical growth direction, became dominant. Meanwhile, all samples exhibited a strong Raman spectrum peak at 314 cm^{-1}, which is attributed to the A_{1g} mode, i.e., the vertical plane lattice vibration mode, of SnS_2 (Fig. 3b). The single peak confirmed the phase purity of SnS_2. To further investigate the microstructure and crystallinity of the 2D SnS_2 nanosheets, a TEM study was performed. The TEM study revealed that most 2D SnS_2 nanosheets were single crystalline with sharp facets (Fig. 3c). The high-resolution TEM image, which was obtained from the corresponding yellow-boxed region in Fig. 3c, showed a lattice spacing of ∼3.2 Å, corresponding to the (100) plane of SnS_2 (Fig. 3d) [27]. The lattice image exhibited a 6-fold rotation axis symmetry, indicating that the lattice image represented the (001) basal plane of the hexagonal SnS_2 structure. Thus, the mainly exposed surfaces of 2D SnS_2 nanosheets were (001) planes, which is consistent with the highest intensity of the (001) peak in the XRD patterns. However, the thin film-like morphology, formed by tightly-packed thick SnS_2 sheets, of 2D SnS_2-VL exhibited a low relative intensity for the (001) peak. The energy-dispersive X-ray spectroscopy (EDX) elemental mapping clearly showed the uniform and homogeneous distribution of elemental Sn and S in the 2D nanosheets (Fig. 3e). An XPS study was performed to examine the chemical states of the 2D SnS_2 nanosheets. Notably, the 2D SnS_2 nanosheets exhibited the almost identical XPS spectra for the Sn 3d and S 2p core levels regardless of the gas ratio of $SnCl_4/H_2S$ (Fig. 3f and g, respectively). The peaks at 486.6 eV and 495.0 eV are attributed to Sn $3d_{5/2}$ and Sn $3d_{3/2}$ of SnS_2, respectively [28,29]. The single Gaussian peaks also indicated the phase purity of SnS_2. In addition, the peaks at 161.6 eV and 162.8 eV corresponded to S $2P_{3/2}$ and S $2P_{1/2}$ of SnS_2, respectively.

The PEC activities of the SnS_2 nanosheets were evaluated in 0.5 M Na_2SO_4 solution by recording the linear sweep voltammograms under repetitive on–off switching of simulated AM 1.5G illumination (Fig. 4a). The photocurrent density kept increasing upon increasing the bias potential. However, the dark current became considerable above 1.3 V, which was attributed to the electrocatalysis and electrocorrosion in solution [24,30]. Interestingly, 2D SnS_2−M exhibited the highest photocurrent density. Fig. 4b shows the apparent effect of SnS_2 microscopic size on PEC reactivity. 2D SnS_2−M showed the highest photocurrent density of ∼240 μA/cm^2, whereas 2D SnS_2-L and 2D SnS_2-VL, which possessed larger SnS_2 nanosheets, yielded significantly lower photocurrent densities of

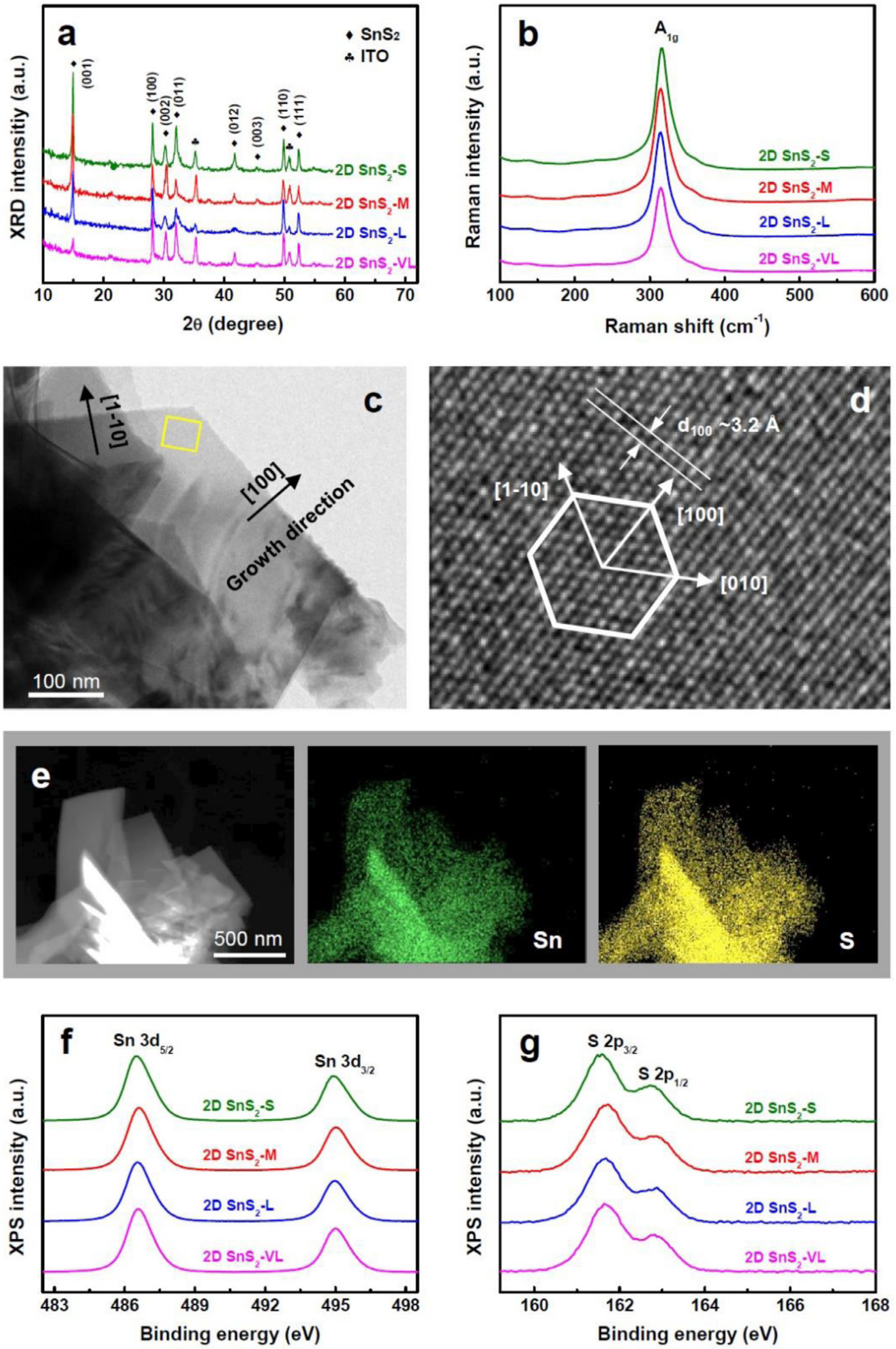

Fig. 3. (a) XRD patterns and (b) Raman spectra of 2D SnS_2-S, 2D SnS_2−M, 2D SnS_2-L, and 2D SnS_2-VL. (c) Low-magnification, (d) high-resolution lattice, and (e) EDX elemental mapping TEM images of 2D SnS_2−M. XPS spectra of (f) Sn 3d and (g) S 2p core levels of 2D SnS_2-S, 2D SnS_2−M, 2D SnS_2-L, and 2D SnS_2-VL.

~150 μA/cm2 and ~105 μA/cm^2, respectively. 2D SnS_2-S, which had the smallest and thinnest SnS_2 nanosheets, exhibited the lowest photocurrent density of ~90 μA/cm^2.

To further understand the 2D SnS_2 nanosheet microscopic structure dependency of the PEC properties, systematic studies, including EIS, UV–vis absorption, and TRPL spectroscopy, were conducted. Fig. 5a and b show the EIS spectra of the 2D SnS_2 samples in the dark and under illumination, respectively. The Nyquist plots were fitted using a simplified Randles circuit (inset of Fig. 5a), which consists of the charge transfer resistance (R_{ct}), solution resistance (R_s), constant phase element (Q), and diffusion of species in the electrolyte solution represented by the Warburg impedance (W). The R_{ct} values are provided in Table S1 in Supporting Information. 2D SnS_2-S exhibited the largest radius of the EIS semicircle, indicating the highest charge transfer resistance in the dark (R_{ct} (dark) ~ 314 kΩ), whereas 2D SnS_2-VL showed the smallest radius (R_{ct} (dark) ~ 17 kΩ). 2D SnS_2−M and 2D SnS_2-L possessed significantly lower R_{ct} (dark) values of ~53 kΩ and ~55 kΩ, respectively, than 2D SnS_2-S. Under illumination, the EIS semicircle curvatures decreased owing to the contribution of

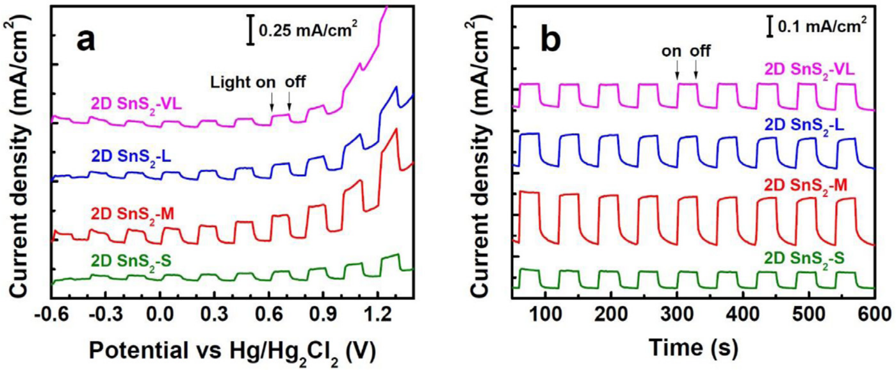

Fig. 4. (a) Photocurrent density–potential and (b) photocurrent density–time curves for PEC cells with various working electrodes (2D SnS_2-S, 2D SnS_2−M, 2D SnS_2-L, and 2D SnS_2-VL) in 0.5 M Na_2SO_4 solution under repetitive on–off switching of simulated AM 1.5 G illumination.

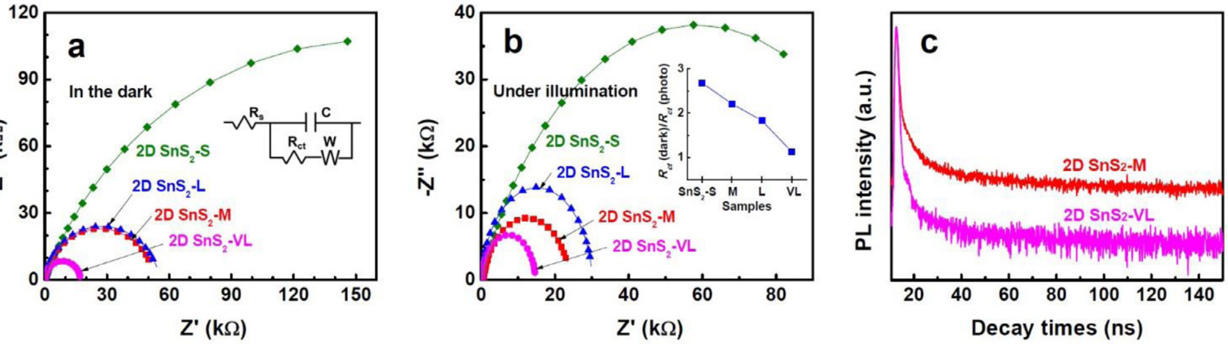

Fig. 5. Nyquist plots of 2D SnS_2-S, 2D SnS_2−M, 2D SnS_2-L, and 2D SnS_2-VL (a) in the dark and (b) under illumination. The inset in (a) shows an equivalent Randles circuit. (c) TRPL results of 2D SnS_2−M and 2D SnS_2-VL.

photogenerated charge carriers (Fig. 5b). Notably, the R_{ct} (dark)/R_{ct} (photo) ratio continued decreasing with increasing size of the 2D SnS_2 nanosheets (inset of Fig. 5b). 2D SnS_2-S still possessed a high R_{ct} (photo) value of ∼117 kΩ, despite having the highest R_{ct} (dark)/R_{ct} (photo) ratio of 2.68. 2D SnS_2-VL had the lowest R_{ct} (dark)/R_{ct} (photo) ratio of 1.13, indicating the smallest gain by photogeneration of electron–hole (e–h) pairs. Of note, 2D SnS_2−M had a lower R_{ct} (photo) value of ∼24 kΩ than 2D SnS_2-L (∼30 kΩ) owing to its higher R_{ct} (dark)/R_{ct} (photo) ratio of 2.21.

The R_{ct} (dark) value difference between the samples is mainly determined by the ITO surface coverage of the 2D SnS_2 nanosheets, i.e., the specific interface area of ITO/SnS_2. The larger specific interface area of thick 2D SnS_2 nanosheets results in a smaller R_{ct} value. Meanwhile, the R_{ct} (photo) values are crucially affected by the charge carrier dynamics, including the photogeneration rate of the e–h pairs upon light absorption and the transport efficiency of the carriers. The highest R_{ct} (dark)/R_{ct} (photo) ratio of 2D SnS_2-S indicates that photogenerated carriers efficiently transfer to the electrode with suppressed recombination. In the thinnest SnS_2 nanosheets, most e–h pairs are photogenerated near the surface and edges so that the e–h pairs can be readily separated from each other by the built-in surface potential. The carriers also have a shorter migration length to surface catalytic sites for PEC reaction [31]. Moreover, charge carriers are transported more efficiently to the electrode along the highly conductive surface and edges than through the bulk interior [32]. Nevertheless, the small specific interface area of 2D SnS_2-S resulted in the highest R_{ct} (dark) and R_{ct} (photo) values, which were a decisive factor for the significantly poor PEC efficiency. In contrast, the bulk-like coverage of 2D SnS_2-VL showed the lowest R_{ct} (dark) value. However, more e–h pairs not only are photogenerated inside the thick SnS_2 nanosheets than near the surface but also migrate through the inefficient bulk interior. Thus, a poor PEC efficiency and the lowest R_{ct} (dark)/R_{ct} (photo) ratio of 1.13 were observed. Obviously, the thickness of the SnS_2 nanosheets should be optimized by balancing a low interfacial contact resistance with effective photogenerated carrier dynamics. Of the samples, 2D SnS_2−M with ∼70-nm-thick SnS_2 nanosheets had a relatively low R_{ct} (dark) value of ∼53 kΩ with a high R_{ct} (dark)/R_{ct} (photo) ratio of 2.21, resulting in the highest PEC performance.

A TRPL spectroscopy study was conducted to understand the dynamic behavior of photogenerated carriers (Fig. 5c). The average carrier lifetimes were extracted by the PL decay kinetics fitted by a bi-exponential decay profile [33]. Compared to 2D SnS_2-VL (0.75 ns), 2D SnS_2−M showed a longer minority carrier lifetime of 1.7 ns. The slow PL decay, i.e., long carrier lifetime, can be attributed to suppressed e–h recombination through efficient separation and transportation of charge carriers. The estimated carrier lifetime of 0.75−1.7 ns is consistent with the reported value for single-crystalline SnS_2 flakes [11,34]. Assuming the intrinsic mobility of single-crystalline SnS_2 flakes (∼300 cm^2 V^{-1} s^{-1}) [11], the carrier diffusion length was estimated to be ∼0.7−1.1 μm. A significant amount of carriers, which are photogenerated in the upper region of SnS_2 nanosheets beyond the carrier diffusion length, cannot efficiently contribute to PEC reaction. Of the samples, 2D SnS_2−M and 2D SnS_2-L had the optimal height corresponding to nearly the limit of the carrier diffusion length. However, 2D SnS_2−M exhibited significantly higher PEC reactivity than 2D SnS_2-L because 2D SnS_2−M had a thickness of ∼70 nm that effectively manifests nanosized effects, such as efficient separation and transportation of photogenerated e−h pairs with suppressed recombination.

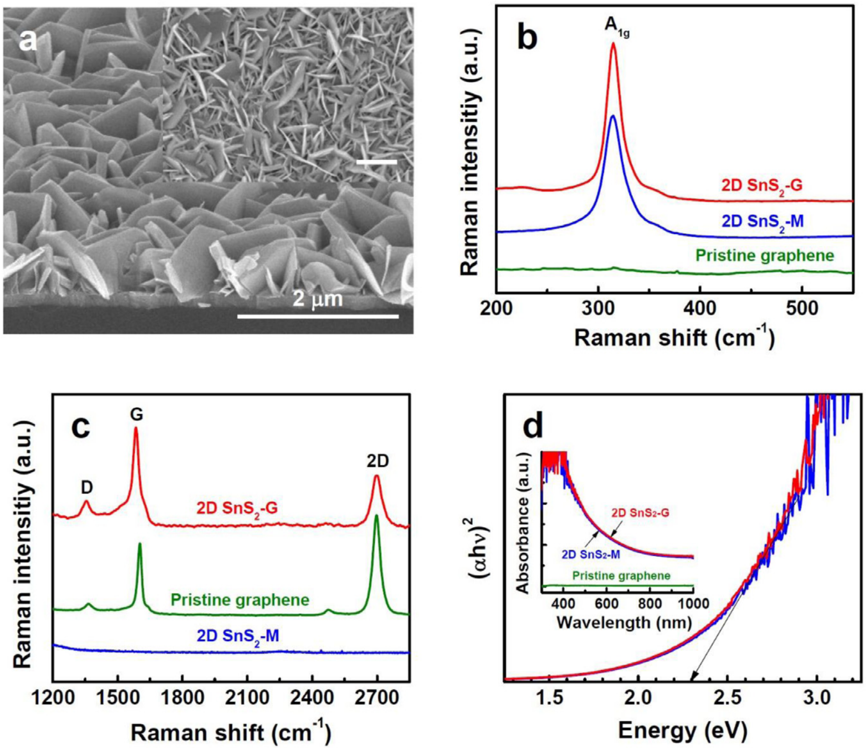

Fig. 6. (a) SEM image of 2D SnS_2 vertically grown on a graphene substrate (2D SnS_2-G). Scale bar is 2 μm. (b) and (c) Raman spectra of graphene, 2D SnS_2-G, and 2D SnS_2–M. (d) Plots of $(\alpha h\nu)^2$ as a function of hν of 2D SnS_2-G and 2D SnS_2–M. The inset in (d) shows the corresponding UV–vis absorption spectra.

To further enhance the PEC performance of 2D SnS_2 nanosheets, they were grown vertically on graphene substrates under the same conditions as 2D SnS_2–M. The 2D SnS_2 nanosheets on graphene, hereinafter referred to as 2D SnS_2-G, showed nearly the same microscopic structure as 2D SnS_2–M (Fig. 6a). The Raman spectrum of 2D SnS_2-G also exhibited a single characteristic peak at 314 cm^{-1}, which is almost identical to that of 2D SnS_2–M (Fig. 6b). Owing to the low-temperature growth at 230 °C, the graphene layer was still present after MOCVD growth of SnS_2, which was confirmed by the presence of characteristic G and 2D band peaks in the Raman spectrum (Fig. 6c). Compared to pristine graphene, 2D SnS_2-G showed an increased I_D/I_G of ~0.17 and a decreased intensity ratio of 2D to G peaks owing to the surface coverage of SnS_2. The CVD-grown graphene exhibited a low intensity ratio of characteristic D to G band peaks (I_D/I_G of ~0.1), indicating a high-quality graphene structure (Fig. 6c). The graphene showed excellent light transmittance of ~96.9% at 550 nm, corresponding to approximately one and a half layers of ideal graphene. Fig. 6d shows the UV–vis absorption spectra of 2D SnS_2–M and 2D SnS_2-G. Both samples showed almost identical light absorption characteristics, except for the slight light absorption difference from the graphene layer (~3%). The samples exhibited a bandgap energy of 2.30 eV, which was estimated from the intercept of the linear portion of the plot of $(\alpha h\nu)^2$ as a function of energy ($h\nu$).

Fig. 7a shows the linear sweep voltammograms of 2D SnS_2–M and 2D SnS_2-G in 0.5 M Na_2SO_4 solution under repetitive on–off switching of simulated AM 1.5G illumination. Both samples exhibited a significant photocurrent density even at zero bias potential. With increasing the bias potential, the photocurrent density of 2D SnS_2-G increased more steeply than that of 2D SnS_2–M. Eventually, 2D SnS_2-G yielded approximately two times higher photocurrent density than 2D SnS_2–M above 0.8 V. This considerably enhanced PEC activity was mainly attributed to the improved charge transfer properties upon insertion of the graphene layer. Fig. 7b shows the IPCE plots of two working electrodes (2D SnS_2–M and 2D SnS_2-G). 2D SnS_2-G exhibited significantly improved photoconversion efficiencies over the overall incident-light waveband, suggesting fortified carrier photogeneration and transfer dynamics. The maximum photoconversion efficiencies of 9.2% and 15.0% were achieved at 360 nm for 2D SnS_2–M and 2D SnS_2-G, respectively. The photoconversion efficiency and photocurrent density of 2D SnS_2-G were at least comparable with various SnS_2 photoanodes reported recently, such as SnS_2/$CuInS_2$ nanosheet films [35], Al-doped ZnO inverse opal shell/SnS_2 core-shell structures [36] and SnO_2/SnS_2 heterojunctions [37,38]. As shown in Fig. 7c and Table S1, the EIS Nyquist plot of 2D SnS_2-G exhibited lower R_{ct} (dark) and R_{ct} (photo)values (49 kΩ and 18 kΩ, respectively) than those of 2D SnS_2–M. The results indicate significantly improved charge transfer properties across the interface between SnS_2 nanosheets and ITO by inserting a graphene layer. The graphene layer not only acts as an excellent conducting layer [16] but also forms a favorable heterojunction with SnS_2 for efficient carrier transport. Notably, the R_{ct} (dark) to R_{ct} (photo) ratio of 2D SnS_2-G was significantly improved to 2.72, suggesting that the graphene/SnS_2 heterojunction was more beneficial under illumination than in the dark.

To gain insight into the carrier transport property across the heterojunction of graphene/SnS_2, its electronic structure was studied via UPS. The work function of SnS_2 (4.45 ± 0.15 eV) was determined on the basis of the difference between the photon energy of excited radiation (21.2 eV) and the spectrum width which is measured from the valence band and secondary edges (16.75 eV, Fig. 8a). The energy difference between the Fermi energy and valence band edge (E_F–E_{VB}) was 1.90 eV (Fig. 8b). Given the bandgap energy of ~2.30 eV for SnS_2 based on the UV–Vis absorption spectrum, the electron affinity of SnS_2 was approximately 4.05 eV (inset in Fig. 8b). This electronic structure suggests the n-type behavior of SnS_2, which works as a photoanode. As shown in Fig. 8c, the Fermi level (~4.6–4.8 eV of work function) of pristine few-layer graphene [39] was appropriately located between the Fermi level of the ITO and the conduction band edge of SnS_2 for efficient extraction of

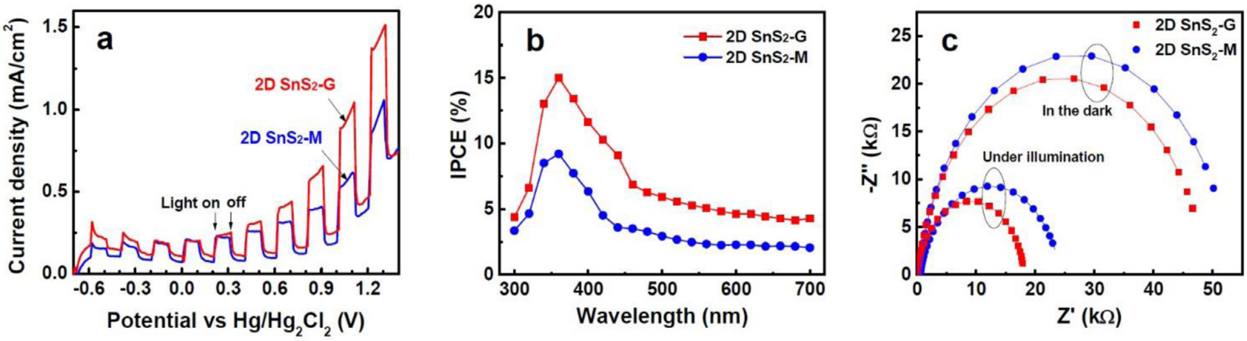

Fig. 7. (a) Photocurrent density–potential for PEC cells with 2D SnS_2-G and 2D SnS_2−M as the working electrode in 0.5 M Na_2SO_4 solution under repetitive on–off switching of simulated AM 1.5 G illumination. (b) IPCE plots and (c) Nyquist plots of the corresponding PEC cells.

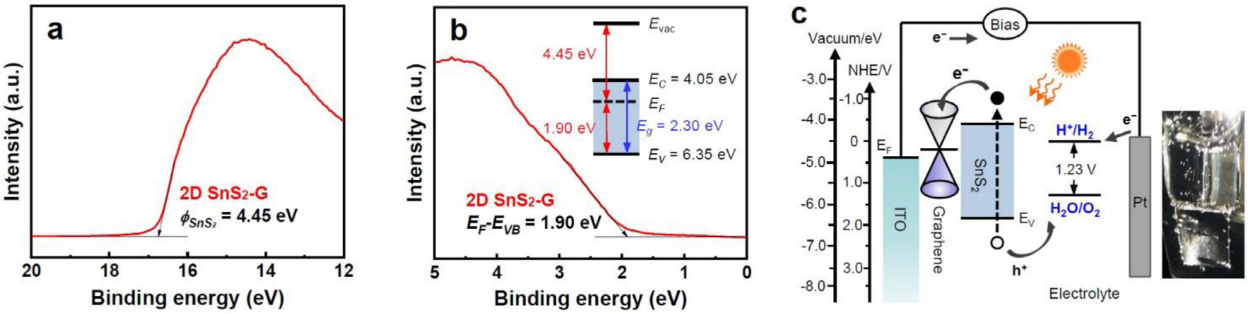

Fig. 8. (a) UPS secondary electron cut-off and (b) valence spectra of 2D SnS_2-G. The inset in (b) shows the corresponding energy band diagram of 2D SnS_2 nanosheets on graphene. (c) PEC water-splitting working principle of 2D SnS_2 nanosheets on graphene. The photo image in (c) shows gas bubbling on the dark cathode (Pt) for 2D SnS_2-G during PEC measurement.

electrons to the cathode. A significant amount of gas bubbles was observed from both the photoanode (SnS_2) and the dark cathode (Pt) during PEC measurement, suggesting that the photocurrent can be attributed to a water-splitting reaction (Fig. 8c).

4. Conclusions

We demonstrated the vertical growth of 2D SnS_2 nanosheets on graphene substrates using MOCVD. Owing to the low temperature growth at 230 °C, the graphene layer was still present after SnS_2 growth and significantly reduced the charge transfer resistance. As a result, 2D SnS_2-G showed approximately two times higher photocurrent density than 2D SnS_2−M. In addition, the microscopic structure of the 2D SnS_2 nanosheets was successfully controlled by the ratio of $SnCl_4/H_2S$. The systematic microscopic structure dependency PEC studies revealed that the following sizes of 2D SnS_2 nanosheets were optimal: a height of ~0.85 µm, corresponding to nearly the limit of the carrier diffusion length, and a thickness of ~70 nm that not only exhibits a reasonably low R_{ct} (dark) value but also effectively manifests nanosized effects, such as efficient separation of photogenerated e–h pairs by the built-in surface potential and fast carrier transportation along the surface and edges of the 2D nanosheets. These results, including the vertical growth of 2D SnS_2 on graphene, provide a promising path for exploiting the full potential of 2D SnS_2 for various PEC applications.

Declaration of Competing Interest

The authors declare that they have no known competing financial interests or personal relationships that could have appeared to influence the work reported in this paper.

CRediT authorship contribution statement

Dong-Bum Seo: Conceptualization, Methodology, Data curation, Software, Writing - original draft. **Tran Nam Trung:** Software. **Eui-Tae Kim:** Supervision, Conceptualization, Visualization, Data curation, Writing - review & editing.

Acknowledgements

This work was supported by the National Research Foundation of Korea (NRF) grants funded by the Ministry of Education (2020R1I1A3A04037241 and 2019R1A6A3A13095792) and the Korea government (MSIT) (2020R1A4A4079397).

Supplementary materials

Supplementary material associated with this article can be found, in the online version, at doi:10.1016/j.electacta.2020.137164.

References

[1] M.G. Walter, E.L. Warren, J.R. Mckone, S.W. Boettcher, Q.X. Mi, E.A. Santori, N.S. Lewis, Solar water splitting cells, Chem. Rev. 110 (2010) 6446–6473.
[2] S. Dahl, I. Chorkendorff, Solar-fuel generation: towards practical implementation, Nat. Mater. 11 (2012) 100–101.
[3] J.W. Sun, D.K. Zhong, D.R. Gamelin, Composite photoanodes for photoelectrochemical solar water splitting, Energy Environ. Sci. 3 (2010) 1252–1261.
[4] M. Zhou, X.W. Lou, Y. Xie, Two-dimensional nanosheets for photoelectrochemical water splitting: possibilities and opportunities, Nano Today 8 (2013) 598–618.
[5] Q. Ding, B. Song, P. Xu, S. Jin, Efficient electrocatalytic and photoelectrochemical hydrogen generation using MoS_2 and related compounds, Chemistry 1 (2016) 699–726.
[6] B. Han, Y.H. Hu, MoS_2 as a co-catalyst for photocatalytic hydrogen production from water, Energy Sci. Eng. 4 (2016) 285–304.
[7] Y. Sun, H. Cheng, S. Gao, Z. Sun, Q. Liu, Q. Liu, F. Lei, T. Yao, J. He, S. Wei, Y. Xie, Freestanding tin disulfide single-layers realizing efficient visible-light water splitting, Angew. Chem. Int. Ed. 51 (2012) 8727–8731.

[8] J. Yu, C.-Y. Xu, F.-X. Ma, S.-P. Hu, Y.-W. Zhang, L. Zhen, Monodisperse SnS_2 nanosheets for high-performance photocatalytic hydrogen generation, ACS Appl. Mater. Interfaces 6 (2014) 22370–22377.

[9] G. Liu, Z. Li, T. Hasan, X. Chen, W. Zheng, W. Feng, D. Jia, Y. Zhou, P. Hu, Vertically aligned two-dimensional SnS_2 nanosheets with a strong photon capturing capability for efficient photoelectrochemical water splitting, J. Mater. Chem. A 5 (2017) 1989–1995.

[10] L. Chen, E. Liu, F. Teng, T. Zhang, J. Feng, Y. Kou, Q. Sun, J. Fan, X. Hu, H. Miao, Two-dimensional SnS_2 nanosheets arrays as photoelectrode by low temperature CVD method for efficient photoelectrochemical water splitting, Appl. Surf. Sci. 467–468 (2019) 698–707.

[11] B. Giri, M. Masroor, T. Yan, K. Kushnir, A.D. Carl, C. Doiron, H. Zhang, Y. Zhao, A. McClelland, G.A. Tompsett, D. Wang, R.L. Grimm, L.V. Titova, P.M. Rao, Balancing light absorption and charge transport in vertical SnS_2 nanoflake photoanodes with stepped layers and large intrinsic mobility, Adv. Energy Mater. 9 (2019) 1901236.

[12] X.S. Jia, C.C. Tang, R.H. Pan, Y.Z. Long, C.Z. Gu, J.J. Li, Thickness-dependently enhanced photodetection performance of vertically grown SnS_2 nanoflakes with large size and high production, ACS Appl. Mater. Interfaces 10 (2018) 18073–18081.

[13] E. Zhao, L. Gao, S. Yang, L. Wang, J. Cao, T. Ma, In situ fabrication of 2D SnS_2 nanosheets as a new electron transport layer for perovskite solar cells, Nano Res. 11 (2018) 5913–5923.

[14] C.W. Shi, P.F. Yang, M. Yao, X.Y. Dai, Z. Chen, Preparation of SnS_2 thin films by close-spaced sublimation at different source temperatures, Thin Solid Films 534 (2013) 28–31.

[15] A. Voznyi, V. Kosyak, A. Opanasyuk, N. Tirkusova, L. Grase, A. Medvids, G. Mezinskis, Structural and electrical properties of SnS_2 thin films, Mater. Chem. Phys. 173 (2016) 52–61.

[16] A.K. Geim, K.S. Novoselov, The rise of graphene, Nat. Mater. 6 (2007) 183–191.

[17] Y. Jiang, D. Song, J. Wu, Z. Wang, S. Huang, Y. Xu, Z. Chen, B. Zhao, J. Zhang, Sandwich-like SnS_2/graphene/SnS_2 with expanded interlayer distance as high-rate lithium/sodium-ion battery anode materials, ACS Nano 13 (2019) 9100–9111.

[18] D. Kong, H. He, Q. Song, B. Wang, Q.H. Yang, L. Zhi, A novel SnS_2@graphene nanocable network for high-performance lithium storage, RSC Adv. 4 (2014) 23372–23376.

[19] Z. Zang, X. Zeng, M. Wang, W. Hu, C. Liu, X. Tang, Tunable photoluminescence of water-soluble AgInZnS-grapheneoxide (GO) nanocomposites and their application in-vivo bioimaging, Sens. Actuators B Chem. 252 (2017) 1179–1186.

[20] X. Liu, T. Xu, Y. Li, Z. Zang, X. Peng, H. Wei, W. Zha, F. Wang, Enhanced X-ray photon response in solution-synthesized $CsPbBr_3$ nanoparticles wrapped by reduced graphene oxide, Sol. Energy Mater. Sol. Cells 187 (2018) 249–254.

[21] J. Wei, Z. Zang, Y. Zhang, M. Wang, J. Du, X. Tang, Enhanced performance of light-controlled conductive switching in hybrid cuprous oxide/reduced graphene oxide (Cu_2O/rGO) nanocomposites, Opt. Lett. 42 (2017) 911–914.

[22] M. Velický, M.A. Bissett, C.R. Woods, P.S. Toth, T. Georgiou, I.A. Kinloch, K.S. Novoselov, R.A.W. Dryfe, Photoelectrochemistry of pristine mono- and few-layer MoS_2, Nano Lett. 16 (2016) 2023–2032.

[23] L.V. Nang, E.T. Kim, Controllable synthesis of high-quality graphene using inductively-coupled plasma chemical vapor deposition, J. Electrochem. Soc. 159 (2012) K93–K96.

[24] T.N. Trung, D.B. Seo, N.D. Quang, D. Kim, E.T. Kim, Enhanced photoelectrochemical activity in the heterostructure of vertically aligned few-layer MoS_2 flakes on ZnO, Electrochim. Acta 260 (2018) 150–156.

[25] D.B. Seo, S. Kim, T.N. Trung, D. Kim, E.T. Kim, Conformal growth of few-layer MoS_2 flakes on closely-packed TiO_2 nanowires and their enhanced photoelectrochemical reactivity, J. Alloy. Compd. 770 (2019) 686–691.

[26] H. Zhang, Y. Balaji, A.N. Mehta, M. Heyns, M. Caymax, I. Radu, W. Vandervorstbd, A. Delabie, Formation mechanism of 2D SnS_2 and SnS by chemical vapor deposition using $SnCl_4$ and H_2S, J. Mater. Chem. C 6 (2018) 6172–6178.

[27] G. Su, V.G. Hadjiev, P.E. Loya, J. Zhang, S. Lei, S. Maharjan, P. Dong, P.M. Ajayan, J. Lou, H. Peng, Chemical vapor deposition of thin crystals of layered semiconductor SnS_2 for fast photodetection application, Nano Lett. 15 (2015) 506–513.

[28] X. An, J.C. Yu, J. Tang, Biomolecule-assisted fabrication of copper doped SnS_2 nanosheet–reduced graphene oxide junctions with enhanced visible-light photocatalytic activity, J. Mater. Chem. A 2 (2014) 1000–1005.

[29] R.K. Chava, J.Y. Do, M. Kang, Enhanced photoexcited carrier separation in CdS-SnS_2 heteronanostructures: a new 1D-0D visible-light photocatalytic system for the hydrogen evolution reaction, J. Mater. Chem. A 7 (2019) 13614–13628.

[30] K. Chang, Z. Mei, T. Wang, Q. Kang, S. Ouyang, J. Ye, MoS_2/Graphene cocatalyst for efficient photocatalytic H_2 evolution under visible light irradiation, ACS Nano 8 (2014) 7078–7087.

[31] S. Linic, P. Christopher, D.B. Ingram, Plasmonic-metal nanostructures for efficient conversion of solar to chemical energy, Nat. Mater. 10 (2011) 911–921.

[32] A.B. Laursen, S. Kegnæs, S. Dahla, I. Chorkendorff, Molybdenum sulfides—efficient and viable materials for electro - and photoelectrocatalytic hydrogen evolution, Energy Environ. Sci. 5 (2012) 5577–5591.

[33] J.D. Major, M. Al Turkestani, L. Bowen, M. Brossard, C. Li, P. Lagoudakis, S.J. Pennycook, L.J. Phillips, R.E. Treharne, K. Durose, In-depth analysis of chloride treatments for thin-film CdTe solar cells, Nat. Commun. 7 (2016) 13231.

[34] Y.-B. Yang, J.K. Dash, A.J. Littlejohn, Y. Xiang, Y. Wang, J. Shi, L.H. Zhang, K. Kisslinger, T.-M. Lu, G.-C. Wang, Large single crystal SnS_2 flakes synthesized from coevaporation of Sn and S, Cryst. Growth Des. 16 (2016) 961–973.

[35] F. Zhang, Y. Chen, W. Zhou, C. Ren, H. Gao, G. Tian, Hierarchical SnS_2/$CuInS_2$ nanosheet heterostructure films decorated with C_{60} for remarkable photoelectrochemical water splitting, ACS Appl. Mater. Interfaces 11 (2019) 9093–9101.

[36] W. Hu, N.D. Quang, S. Majumder, E. Park, D. Kim, H.-S. Choi, H.S. Chang, Efficient photo charge transfer of Al-doped ZnO inverse opal shells in SnS_2 photoanodes prepared by atomic layer deposition, J. Alloy. Compd. 819 (2020) 153349.

[37] J. Mu, F. Teng, H. Miao, Y. Wang, X. Hu, In-situ oxidation fabrication of 0D/2D SnO_2/SnS_2 novel Step-scheme heterojunctions with enhanced photoelectrochemical activity for water splitting, Appl. Surf. Sci. 501 (2020) 143974.

[38] F. Wu, Z. Wang, C. Zhang, B. Luo, M. Xiao, S. Wang, A. Du, L. Li, L. Wang, Two-dimensional heterojunction SnS_2/SnO_2 photoanode with excellent photoresponse up to near infrared region, Sol. Energy Mater. Sol. Cells 207 (2020) 110342.

[39] Y.J. Yu, Y. Zhao, S. Ryu, L.E. Brus, K.S. Kim, P. Kim, Tuning the graphene work function by electric field effect, Nano Lett. 9 (2009) 3430–3434.

Supporting Information for

Controllable low-temperature growth and enhanced photoelectrochemical water splitting of vertical SnS_2 nanosheets on graphene

Dong-Bum Seo, Min-Song Kim, Tran Nam Trung, and Eui-Tae Kim*

Department of Materials Science & Engineering, Chungnam National University, Daejeon 34134, Republic of Korea

* To whom correspondence should be addressed; E-mail: etkim@cnu.ac.kr

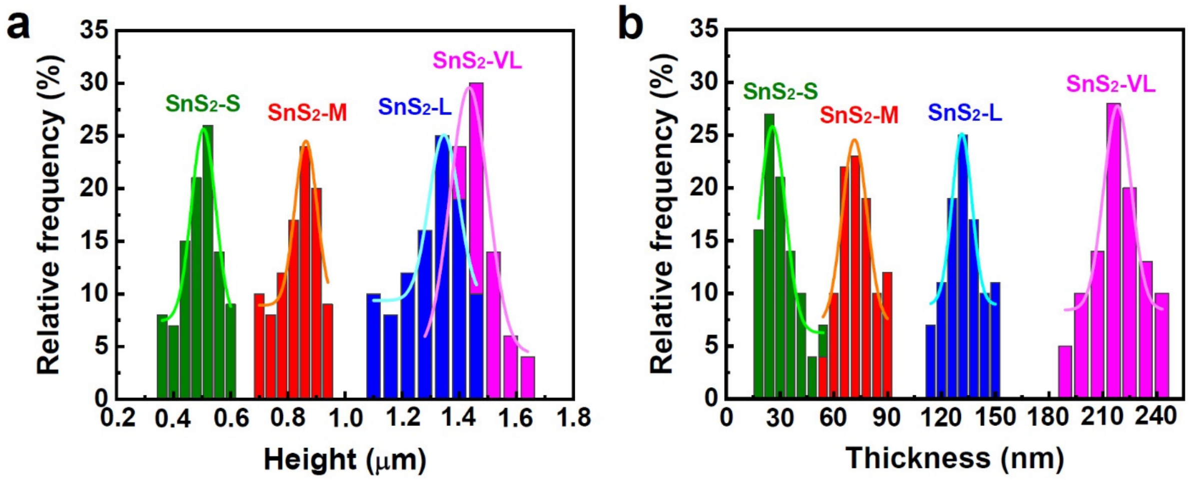

Fig. S1. Height and thickness distributions of 2D SnS_2-S, 2D SnS_2-M, 2D SnS_2-L, and 2D SnS_2-VL.

Table S1. R_{ct} values for EIS analysis in the dark and under illumination.

Samples	R_{ct} (dark) [kΩ]	R_{ct} (photo) [kΩ]	R_{ct} (dark)/R_{ct} (photo)
2D SnS_2-S	314	117	2.68
2D SnS_2-M	53	24	2.21
2D SnS_2-L	55	30	1.83
2D SnS_2-VL	17	15	1.13
2D SnS_2-G	49	18	2.72